

# Efficient Vacuum-Processed Light-Emitting Diodes Based on Carbene–Metal–Amides

Patrick J. Conaghan, S. Matthew Menke, Alexander S. Romanov, Saul T. E. Jones, Andrew J. Pearson, Emrys W. Evans, Manfred Bochmann, Neil C. Greenham, and Dan Credgington\*

Efficient vacuum-processed organic light-emitting diodes are fabricated using a carbene–metal–amide material, CMA1. An electroluminescence (EL) external quantum efficiency of 23% is achieved in a host-free emissive layer comprising pure CMA1. Furthermore external quantum efficiencies of up to 26.9% are achieved in host–guest emissive layers. EL spectra are found to depend on both the emissive-layer doping concentration and the choice of host material, enabling tuning of emission color from mid-green (Commission Internationale de l'Éclairage co-ordinates [0.24, 0.46]) to sky blue ([0.22 0.35]) without changing dopant. This tuning is achieved without compromising luminescence efficiency (>80%) while maintaining a short radiative lifetime of triplets (<1 μs).

Organic light-emitting devices (OLEDs) have been studied for over 30 years<sup>[1]</sup> and a central research theme has been the design of new dopants to overcome spin-statistical electroluminescence (EL) efficiency limits.<sup>[2,3]</sup> In a conventional, fluorescent OLED only 25% of electron–hole recombination events will result in EL, as 75% of recombination events lead to the formation of non-emissive triplet excitons. Triplet excitons tend to have low rates of radiative decay and the exchange energy between singlet and triplet exciton states is too great to allow efficient reverse inter-system crossing (RISC) from the lower-energy triplet state to the higher-energy singlet state. Recently, organic semiconductors exhibiting thermally activated delayed fluorescence (TADF) have been used to achieve highly efficient OLEDs by reducing the singlet–triplet energy gap.<sup>[2]</sup> In this case, prompt fluorescence occurs immediately from the singlet state and delayed

fluorescence occurs after one or more cycles of inter-system crossing and RISC between the singlet and triplet manifolds.


A recent report introduced a new class of solution-processable TADF-type dopants based on carbene–metal–amide (CMA) materials.<sup>[4]</sup> CMA materials consist of a cyclic (alkyl)(amino)carbene (CAAC) linked via a metal (typically copper(I) or gold(I)) to a carbazolate or diphenylamide as the amide ligand.<sup>[5]</sup> Both the exchange energy and the oscillator strength in CMA compounds are calculated to depend on the dihedral angle between the carbene and amide ligands about

the C–metal–N axis, and on deformation of the C–metal–N bond.<sup>[4,6–8]</sup> It is typically assumed that to achieve efficient emission, a compromise must be made between exchange energy and oscillator strength. The ability to control the distribution of rotational conformers, for example, through alternative processing methods, may result in emissive layers exhibiting different photophysical properties, which in turn will affect device performance. Champion solution-processed host–guest CMA devices have EL external quantum efficiencies ( $\eta_{\text{EQE,EL}}$ ) up to 27.5%, yet exhibit large device-to-device variation, with the average peak  $\eta_{\text{EQE,EL}}$  closer to 18%. In this work, we use vacuum thermal evaporation, the current industrially preferred OLED fabrication process, to produce OLEDs using the archetypical CMA dopant CMA1. We observe highly efficient OLED performance with champion  $\eta_{\text{EQE,EL}} = 26.9\%$  and substantially reduced device-to-device variation in comparison to solution-processed devices. We also demonstrate  $\eta_{\text{EQE,EL}} > 23\%$  for OLEDs based on a host-free CMA1 emissive layer. This outperforms previously reported host-free TADF OLEDs.<sup>[9]</sup> A clear evolution in EL spectra is observed both as a function of dopant concentration and host material and is distinct from that seen in the solution-processed variants. We attribute these differences to changes in the host environment and molecular degrees of freedom.

OLED devices were fabricated by high-vacuum ( $10^{-7}$  Torr) thermal evaporation on indium tin oxide (ITO)-coated glass substrates with sheet resistance of  $15 \Omega \square^{-1}$ . The OLED device architecture is shown in **Figure 1a** including values of the highest occupied molecular orbital (HOMO) and lowest unoccupied molecular orbital (LUMO) energy levels for the materials used.<sup>[10–12]</sup> A 40 nm thick layer of 1,1-bis[4-[N,N-di(4-tolyl)amino]phenyl]-cyclohexane (TAPC) was used as the electron-blocking and hole-transporting layer. The CMA1 dopant (**Figure 1b**) was co-evaporated in a 1,3-bis(N-carbazolyl)benzene

P. J. Conaghan, Dr. S. M. Menke, S. T. E. Jones, Dr. A. J. Pearson, Dr. E. W. Evans, Prof. N. C. Greenham, Dr. D. Credgington  
Cavendish Laboratory  
University of Cambridge  
JJ Thomson Avenue, CB3 0HE, Cambridge, UK  
E-mail: djnc3@cam.ac.uk

Dr. A. S. Romanov, Prof. M. Bochmann  
School of Chemistry  
University of East Anglia  
Earlham Road, Norwich NR4 7JT, UK

 The ORCID identification number(s) for the author(s) of this article can be found under <https://doi.org/10.1002/adma.201802285>.

© 2018 The Authors. Published by WILEY-VCH Verlag GmbH & Co. KGaA, Weinheim. This is an open access article under the terms of the Creative Commons Attribution License, which permits use, distribution and reproduction in any medium, provided the original work is properly cited.

The copyright line for this article was changed on 20 March 2020 after original online publication.

DOI: 10.1002/adma.201802285

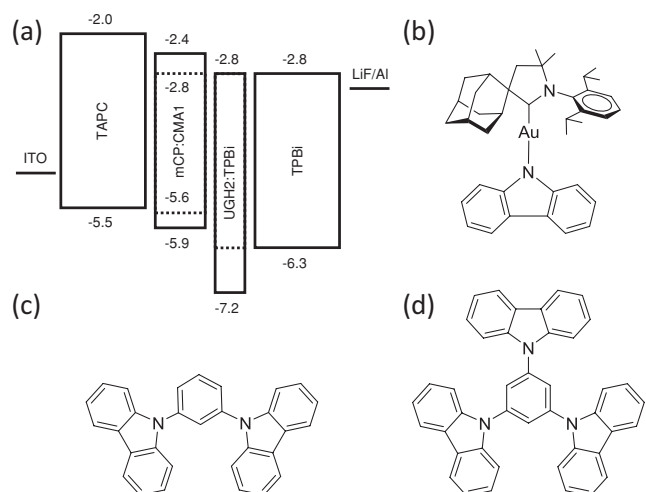


**Figure 1.** a) Device architecture of CMA1 OLEDs ITO/TAPC(40 nm)/mCP:CMA1(20 nm, varying wt%)/UGH2:TPBi(10 nm, 10 wt% TPBi)/TPBi(40 nm)/LiF(1 nm)/Al(100 nm) HOMO and LUMO energy levels are indicated in eV. b–d) Chemical structures of CMA1 (b), mCP (c), and TCP (d).

(mCP, Figure 1c) host at various dopant concentrations between 5 and 100 wt% and in a 1,3,5-tris(carbazol-9-yl)benzene (TCP, Figure 1d) host at 25 wt%. The total emissive layer thickness was kept constant at 20 nm. A 10 nm thick hole-blocking layer of 1,4-bis(triphenylsilyl)benzene (UGH2) was lightly doped with 10 wt% of 1,3,5-tris(2-*N*-phenylbenzimidazole-1-yl)benzene (TPBi) which was found to improve the yield of operational pixels. A 40 nm thick layer of TPBi was used as the electron-transport layer. Chemical structures of the transport and blocking layers are shown in Figure S1 (Supporting Information). The cathode is formed of a 1 nm thick layer of lithium fluoride (LiF) and a 100 nm thick layer of aluminium (Al) evaporated through a shadow mask to define a 4.5 mm<sup>2</sup> pixel area.

**Figure 2** shows the current density–voltage and luminance–voltage characteristics of champion CMA1 evaporated devices with varying dopant concentrations in the emissive layer. Leakage currents at low applied bias are in the range of 10<sup>−5</sup> mA cm<sup>−2</sup> for representative pixels. However, ≈50% of pixels displayed a large leakage current, on the order of 10<sup>−2</sup> mA cm<sup>−2</sup> at forward biases below the EL turn-on. These higher-leakage pixels were excluded from further analysis. The bimodal variation in leakage current is thought to be due to inhomogeneity in the relatively rough UGH2 hole-blocking layer (RMS = 8.6 nm, see Figure S2, Supporting Information),

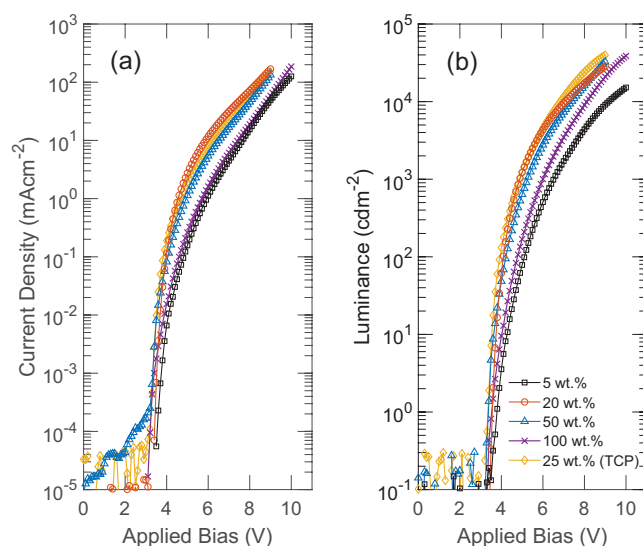


**Figure 2.** a) Current density–voltage and b) luminance–voltage characteristics for devices with varying emissive layer dopant concentration in mCP and TCP hosts.

which in some instances may allow a leakage of holes through the device. The shallow LUMO of CMA1 limits the choice of available hole-blocking materials that could form a smoother layer while still allowing barrier-free electron transfer. As shown in **Table 1**, we observe turn-on voltages (luminance > 1 cd m<sup>−2</sup>) of 4 V or lower for all emissive layer concentrations. This suggests an absence of large barriers to carrier injection, transport through the device, or transfer to the emitting CMA1 molecules.

**Figure 3** shows  $\eta_{\text{EQE,EL}}$  as a function of current density for champion evaporated CMA1 OLEDs with varying emissive layer concentration in a host of mCP. The  $\eta_{\text{EQE,EL}}$  was calculated from on-axis irradiance measurements assuming Lambertian emission, as is commonly observed for planar OLEDs.<sup>[13]</sup> To test the validity of this assumption, the angular distribution of emission was measured and fitted with the function  $\gamma = \cos^n(x)$ , where  $x$  is the emission angle and  $\gamma$  is emission intensity. As shown in Figure S3 (Supporting Information), the  $n$  values fitted for 20 and 50 wt% mCP:CMA1 and 100 wt% CMA1 devices were 0.93, 0.79, and 0.88, respectively. This represents super-Lambertian emission, suggesting the stated values of  $\eta_{\text{EQE,EL}}$  may be slight underestimates. Good roll-off characteristics are observed, especially for the 50 wt% mCP:CMA1 and 100 wt% CMA1 devices where the luminance at 90% of the peak  $\eta_{\text{EQE,EL}}$  ( $L_{90\%}$ ) is 1500 and 2200 cd m<sup>−2</sup>, respectively.

**Table 1.** Summary of champion (average ± standard deviation) OLED turn-on voltage and  $\eta_{\text{EQE}}$  performance at varying EML doping concentration and brightness.

CMA1 concentration [wt%]	$V_{\text{ON}}$ [V]	$\eta_{\text{EQE,EL}}$ [%] (Max.)	$\eta_{\text{EQE,EL}}$ [%] (100 cdm <sup>−2</sup> )	$\eta_{\text{EQE,EL}}$ [%] (1000 cdm <sup>−2</sup> )	CIE (x, y)
5	3.8 (4.0 ± 0.1)	19.8 (17.8 ± 1.6)	18.8 (15.8 ± 1.0)	15.7 (12.6 ± 1.1)	(0.22, 0.35)
20	3.5 (3.6 ± 0.1)	24.3 (22.2 ± 0.8)	22.5 (21.6 ± 0.5)	19.4 (19.3 ± 0.6)	(0.22, 0.36)
50	3.4 (3.4 ± 0.1)	23.4 (22.0 ± 0.9)	23.3 (21.9 ± 0.9)	21.8 (20.7 ± 0.7)	(0.23, 0.38)
100 (Host-free)	3.5 (3.4 ± 0.1)	23.1 (18.5 ± 2.6)	23.0 (18.4 ± 2.7)	22.0 (17.7 ± 2.5)	(0.24, 0.46)
25 (TCP host)	3.3 (3.4 ± 0.1)	26.9 (26.0 ± 0.6)	26.4 (25.6 ± 0.8)	24.9 (24.4 ± 0.6)	(0.24, 0.42)

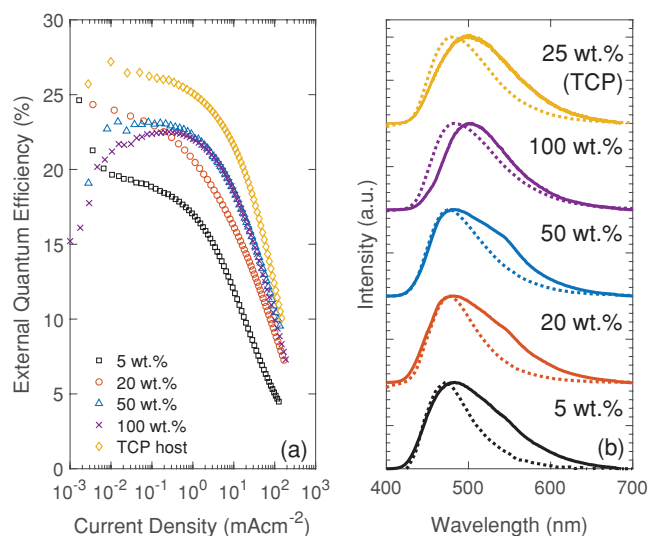


**Figure 3.** a) External quantum efficiency as a function of current density for OLEDs of varying dopant concentration. b) Normalized EL spectra (solid lines) at  $\approx 100 \text{ cd m}^{-2}$  and photoluminescence spectra (dashed lines, excitation wavelength  $\lambda_{\text{ex}} = 390 \text{ nm}$ )

Table 1 shows an average  $\pm$  standard deviation peak  $\eta_{\text{EQE,EL}}$  of  $22.2 \pm 0.8\%$  for the 20 wt% emissive layer and  $22.0 \pm 0.9\%$  for the 50 wt% emissive layer. These high  $\eta_{\text{EQE,EL}}$  values imply very effective triplet harvesting in devices.  $\eta_{\text{EQE,EL}}$  values are also consistently measured to be greater than the limit of 20% commonly assumed for the outcoupling efficiency of planar OLEDs with isotropic transition dipole orientation.<sup>[14]</sup> Favorable molecular alignment can sometimes lead to enhanced outcoupling efficiency.<sup>[15]</sup> However, grazing-incidence wide-angle X-ray scattering (GIWAXS) measurements suggest that when CMA1 is processed into a thin film it forms nanoscale aggregations with limited internal order and only a weak directional preference for molecular packing (Figure S4, Supporting Information). We again note the roughness of the UGH2:TPBi hole blocking layer which may play a role in outcoupling. High  $\eta_{\text{EQE,EL}}$  was observed across a wide range of emissive layer concentrations, including a champion peak  $\eta_{\text{EQE,EL}} = 23.1\%$  for a 100-wt% (i.e., host-free) emissive layer. This implies that the concentration quenching observed for many OLED dopants<sup>[16,17]</sup> is largely absent in CMA1, as has previously been reported for its halide analogues.<sup>[5b]</sup> To investigate this, the absolute photoluminescence quantum efficiency (PLQE)<sup>[18]</sup> was measured under a flow of  $\text{N}_2$  for the 20 and 100 wt% CMA1 films. The 20 wt% film exhibited a PLQE of 86% while the 100 wt% film exhibited a PLQE of 83%. Intermolecular interactions between CMA1 molecules are therefore relatively weak, and nonradiative pathways appear insensitive to the surrounding environment. However, histograms of peak  $\eta_{\text{EQE}}$  (Figure S6, Supporting Information) show that the distribution of performance of 100 wt% devices is multimodal, resulting from good intrabatch reproducibility but increased variability between batches fabricated on different occasions. We attribute this to a greater sensitivity of charge balance and transport to processing conditions in 100 wt% devices. The primary electronic role of the host is therefore likely to be to ensure good charge balance, rather than dilution of guest dopants. The standard deviation of peak  $\eta_{\text{EQE,EL}}$

between pixels is 2.6% for the 100 wt% devices and  $\leq 1.6\%$  for all other emitting layer concentrations. This represents a much improved device-to-device variation in comparison to the previously published solution-processed devices.<sup>[4]</sup>

For dopant concentrations between 5 and 50 wt% in mCP, the EL peak is at  $\lambda = 480 \text{ nm}$  (Figure 3b). With increasing concentration, the emission broadens with an increasing contribution from a shoulder at  $\lambda = 540 \text{ nm}$ . The spectral positions of the peaks at  $\lambda = 480$  and  $540 \text{ nm}$  do not shift appreciably, nor does the emission onset, but a relative change in peak intensity is observed. The 100 wt% device shows unstructured EL peaked at  $\lambda = 500 \text{ nm}$ . This corresponds to a 100 meV change in the peak emission energy between a 20 wt% and 100 wt% device. A shift of 80 meV is observed in the high energy onset of the emission when moving from mCP:CMA1 host-guest to host-free devices. The consequent evolution in Commission Internationale de l'Éclairage (CIE) color co-ordinates is shown in Figure S7 (Supporting Information), which also shows that the EL spectrum of vacuum-processed devices is blueshifted in comparison to the previously reported solution-processed OLEDs.<sup>[4]</sup> The associated steady-state photoluminescence (PL) spectra are presented in Figure 3b exhibiting similar peak positions to the EL.

It has been proposed that reorganization of molecular dipoles plays an important role in the emission of CMA1 in solid host-guest films, since CMA molecules exhibit a large static dipole moment in their ground state which changes sign upon excitation.<sup>[6]</sup> Using photothermal deflection spectroscopy (see Figure S8, Supporting Information), we find evidence for this in a blueshift of the CMA1 absorption edge of  $\approx 30 \text{ meV}$  when CMA is dispersed in mCP host. As found through density functional theory (DFT) calculation, mCP has a static dipole moment of  $\approx 1.4 \text{ D}$ . However, the concomitant blueshift in EL indicates that any reorganization of the host-guest composite to accommodate the excited state dipole occurs on longer timescales than that of luminescence.

To explore this effect further, we replaced the asymmetric host mCP with the symmetric variant TCP with a static dipole moment calculated to be 0.3 D. We find that OLEDs fabricated using a TCP host exhibit EL peak and absorption onset coincident with those of neat CMA1 films (Figure 3b; Figure S8, Supporting Information), suggesting that neat CMA1 behaves as a relatively nonpolar environment. TCP host-guest devices also exhibit systematically higher external quantum efficiency with champion peak  $\eta_{\text{EQE}}$  of 26.9% and good roll-off characteristics with  $L_{90\%} = 1700 \text{ cd m}^{-2}$ .

As shown in Figure 3b, the PL and EL emission peaks are similar which we take to indicate that they originate from similar states. To determine the impact of the evaporated host-guest morphology on emission kinetics and to clarify the role of triplets, we conduct time-resolved PL measurements using an electrically gated intensified charge-coupled device and pulsed laser excitation at  $\lambda_{\text{ex}} = 400 \text{ nm}$  under high vacuum ( $\approx 10^{-5} \text{ Torr}$ ). Figure 4a shows room temperature ( $\approx 295 \text{ K}$ ) PL kinetics of an evaporated 100 wt% CMA1 film and evaporated 20 wt% films in mCP and TCP hosts integrated over all wavelengths. Less than 1% of the total emission occurs in the first 5 ns after excitation; this indicates that prompt singlet emission is quenched. Since the high neat-film PLQE values show the

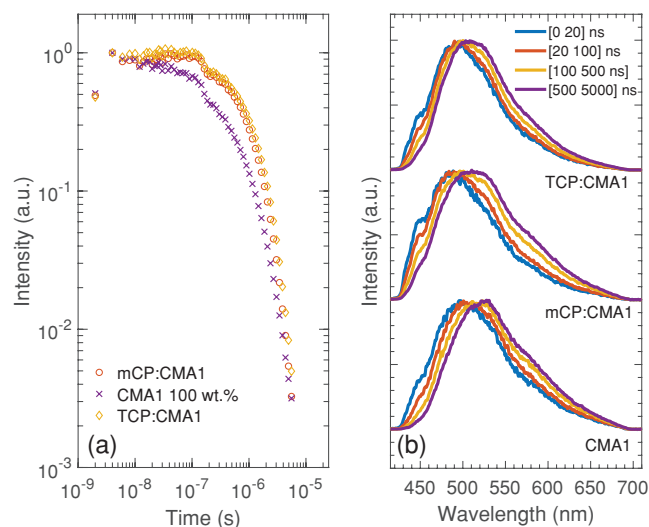


**Figure 4.** a) Transient photoluminescence kinetics and b) transient photoluminescence spectral evolution for a 20 and 100 wt% evaporated film of CMA1 at room temperature.

nonradiative decay rate to be slow, we assign this quenching to rapid intersystem crossing to the triplet state. Subsequent emission must therefore come via the triplet state, such that PL and EL follow similar pathways. Figure S9 (Supporting Information) presents characteristic decay times as a function of temperature for 100 wt% CMA1 films. Emission is found to be thermally activated with an activation energy of 79 meV. This is consistent with a TADF-type emission process, i.e., where the lowest accessible triplet state is weakly coupled to the singlet ground state, but thermal excitation allows access to intermediate states offering stronger coupling to the ground state. Figure 4b shows the emission spectra to be broad and unstructured, consistent with the emissive state having charge-transfer (CT) character. Figure S9 (Supporting Information) shows that PL spectra remain unstructured at all temperatures—i.e., the emissive state retains CT character even in the absence of thermal energy, and no lower-lying ligand-centered “local” triplet is revealed. This is in agreement with existing quantum chemical calculations.<sup>[4,6,8]</sup> The emission energy blueshifts at low temperature, consistent with previous reports,<sup>[4]</sup> which we interpret to mean that relaxation modes for the CT excitons are progressively frozen out. Given the sub-microsecond emission lifetimes at room temperature and the presence of a heavy element, we infer that spin–orbit coupling is the most likely mediating interaction between the triplet and singlet states.

The decay kinetics for 100 wt% CMA1, mCP:CMA1, and TCP:CMA1 at room temperature ( $\approx 295$  K) are nonexponential and the emission spectra redshift over time, consistent with an ensemble of molecular configurations with different intrinsic lifetimes. The characteristic decay time for the ensemble is 755 ns for the 100 wt% film, 881 ns for the mCP host film, and 972 ns for the TCP host film. At room temperature, the PL redshifts between 20 ns and 5  $\mu$ s by  $\approx 135 \pm 10$  meV for the mCP:CMA1 and the 100 wt% CMA1 films and by 84 meV for the TCP:CMA1 film. At early times (0–100 ns), the mCP:CMA1 PL spectrum is blueshifted compared to the 100 wt% and TCP:CMA1 spectra, which is consistent with measurements

of EL and absorption onset. However, at later times (500–5000 ns) the PL of mCP:CMA1 and TCP:CMA1 films both peak at 510 nm (compared to  $\approx 530$  nm for neat CMA1). This spectral diffusion suggests migration of excitons occurs on similar timescales to emission, and is consistent with the relatively high energetic disorder present in the chromophore population indicated by Urbach energies measured (using photothermal deflection spectroscopy) in the  $68 \pm 7$  meV range for all films. This disorder may represent static configurational variation or the ability of individual chromophores to access a range of geometric configurations over time.

In summary, we have demonstrated thermally evaporated OLEDs incorporating a CMA dopant in an mCP host which achieve  $\eta_{\text{EQE,EL}}$  up to 24.3% and good reproducibility between devices. Using a TCP host,  $\eta_{\text{EQE,EL}} > 25\%$  is consistently achieved. Efficient devices with  $\eta_{\text{EQE,EL}}$  up to 23.1% have also been produced using a pure emissive layer, though at a cost to reproducibility. We have shown that the PLQE of evaporated CMA1 films exhibits limited sensitivity to dopant concentration. This insensitivity may offer an insight into the high performance of solution-processed CMA devices previously reported, for which dopant aggregation is difficult to avoid, and explains the surprising effectiveness of host-free evaporated devices. We show that host-free emissive layers exhibit comparably short emission lifetimes than those utilizing dilute guests, with consequent advantages gained through simplification of the manufacturing process, simpler triplet management, and reduced average triplet density in the emissive layer. Reducing average triplet density has previously been shown to extend device lifetime.<sup>[19]</sup> The observed EL spectrum is in all cases distinct and blueshifted from that seen in solution-processed devices, which we consider to arise from the different chromophore morphology achieved through vacuum deposition. We find that host polarity may provide a method to shift both the absorption edge and emission peak of CMA1. We thus conclude that in evaporated device stacks, dynamic reorganization of the solid lattice around an excited molecule is unlikely to occur, at least on the timescale of emission, and that the large ground state dipole of CMA1 does not itself affect the emission wavelength of adjacent excited molecules. We establish that these relatively complex molecules maintain their excellent performance characteristics when employed in a vacuum-deposited architecture. By doing so, we reveal that host environment and deposition conditions provide powerful tools to control, and specifically to blueshift, the emission of CMA archetypes without compromising functionality and maintaining rapid, efficient emission from triplet states.

## Experimental Section

OLED devices were fabricated by high-vacuum ( $10^{-7}$  Torr) thermal evaporation. Prior to deposition of the organic layers, the ITO-coated glass substrates were sonicated in a nonionic detergent, acetone, and propan-2-ol and subject to an oxygen plasma treatment for 10 min. The deposition rate for all organic layers was  $0.2 \text{ nm s}^{-1}$ . A 40 nm thick layer of TAPC was deposited to form the electron-blocking and hole-transporting layer. The CMA1 dopant was co-evaporated in an mCP host at various concentrations between 20 and 100 wt%. The total emissive layer thickness was kept constant at 20 nm. A 10 nm thick hole-blocking layer of UGH2 was lightly doped with 10 wt% of TPBi which was found

to improve the yield of operational pixels. A 40 nm thick layer of TPBi was used as the electron-transport layer. The cathode was formed of a 1 nm thick layer of LiF and a 100 nm thick layer of Al evaporated through a shadow mask to create 4.5 mm<sup>2</sup> pixels. Current-density and voltage measurements were performed using a Keithley 2635 source-meter. The luminance was measured on-axis using a calibrated Si photodiode. The EL and steady-state PL spectra were measured using an Edinburgh Instruments FLS980 spectrometer. EL measurements were made at a constant current of 8  $\mu$ A corresponding to a luminance of  $\approx$ 100 cd m<sup>-2</sup>. Steady-state PL measurements used a monochromated xenon arc lamp as the excitation source with  $\lambda_{\text{ex}} = 390$  nm. GIWAXS measurements were conducted using the beamline I07 at Diamond Light Source in the UK. The energy of the X-ray beam was 10 keV with measured data obtained at the sample critical angle ( $\approx$ 0.2 $^\circ$ ). Films were prepared on Si substrates. Obtained data was calibrated using silver behenate powder and analyzed using the DAWN software package (<http://dawnsci.org>). The PLQE measurements were performed in an integrating sphere under a flow of N<sub>2</sub> using an Andor Shamrock spectrometer and Andor iDus CCD array and laser excitation at  $\lambda_{\text{ex}} = 405$  nm. Photothermal deflection spectroscopy (PDS) measurements were performed using monochromatic pump-light. The absorption-induced deflection of a continuous wave probe laser was measured using a photodiode and lock-in amplifier combination. DFT calculations were performed using the B3LYP functional and 6-31G\* basis set; structures were geometry optimized in vacuum. Time-resolved PL measurements were made under high vacuum using an Andor electrically gated intensified charge-coupled device and laser excitation at  $\lambda_{\text{ex}} = 400$  nm. For low-temperature measurements, an Oxford Instruments continuous flow cryostat was used with liquid helium as the coolant.

## Supporting Information

Supporting Information is available from the Wiley Online Library or from the author.

## Acknowledgements

This work was supported by the Engineering and Physical Sciences Research Council (EPSRC, grant no. EP/M005143/1) and the European Research Council (ERC). P.J.C. acknowledges EPSRC for Ph.D. studentship funding and A.J.P. also acknowledges support from EPSRC (grant no. EP/M024873/1). S.M.M. acknowledges support from the KAUST Competitive Research Grant Program. M.B. is an ERC Advanced Investigator Award holder (Grant No. 338944-GOCAT). D.C. acknowledges the support from the Royal Society (grant nos. UF130278 and RG140472). The authors thank the Diamond Light Source for access to the I07 beamline (session SI7223-1) and for the help during the GIWAXS experiments. The authors thank Mojtaba Abdi-Jalebi for PDS measurements and Edoardo Ruggeri for the help with GIWAXS measurements. The data underlying this publication is available through the following web link: <https://doi.org/10.17863/CAM.24419>.

## Conflict of Interest

The authors declare no conflict of interest.

## Keywords

carbene–metal–amide, host-free, organic light-emitting diodes, thermally activated delayed fluorescence, vacuum-processed

Received: April 10, 2018  
Revised: May 26, 2018  
Published online: July 9, 2018

- [1] C. W. Tang, S. A. Vanslyke, *Appl. Phys. Lett.* **1987**, *51*, 913.
- [2] H. Uoyama, K. Goushi, K. Shizu, H. Nomura, C. Adachi, *Nature* **2012**, *492*, 234.
- [3] M. A. Baldo, D. F. O'Brien, Y. You, A. Shoustikov, S. Sibley, M. E. Thompson, S. R. Forrest, *Nature* **1998**, *395*, 151.
- [4] D. Di, A. S. Romanov, L. Yang, J. M. Richter, J. P. H. Rivett, S. Jones, T. H. Thomas, M. A. Jalebi, R. H. Friend, M. Linnolahti, M. Bochmann, D. Credgington, *Science* **2017**, *356*, 159.
- [5] a) A. S. Romanov, C. R. Becker, C. E. James, D. Di, D. Credgington, M. Linnolahti, M. Bochmann, *Chem. Eur. J.* **2017**, *23*, 4625; b) A. S. Romanov, D. Di, L. Yang, J. Fernandez-Cestau, C. R. Becker, C. E. James, B. Zhu, M. Linnolahti, D. Credgington, M. Bochmann, *Chem. Commun.* **2016**, *52*, 6379.
- [6] J. Föllner, C. M. Marian, *J. Phys. Chem. Lett.* **2017**, *8*, 5643.
- [7] T. J. H. Hele, D. Credgington, *arXiv* **2018**, *1802*, 00804v1.
- [8] E. J. Taffet, Y. Olivier, F. Lam, D. Beljonne, G. D. Scholes, *J. Phys. Chem. Lett.* **2018**, *9*, 1620.
- [9] Q. Zhang, D. Tsang, H. Kuwabara, Y. Hatae, B. Li, T. Takahashi, S. Y. Lee, T. Yasuda, C. Adachi, *Adv. Mater.* **2015**, *27*, 2096.
- [10] Y. Yang, P. Cohn, A. L. Dyer, S. Eom, J. R. Reynolds, R. K. Castellano, J. Xue, *Chem. Mater.* **2010**, *22*, 3580.
- [11] R. J. Holmes, B. W. D'Andrade, S. R. Forrest, X. Ren, J. Li, M. E. Thompson, *Appl. Phys. Lett.* **2003**, *83*, 3818.
- [12] H. Etori, T. Yasuda, X. L. Jin, K. Fujita, S. Mataka, T. Tsutsui, *Jpn. J. Appl. Phys.* **2007**, *46*, 5071.
- [13] N. C. Greenham, R. H. Friend, D. D. C. Bradley, *Adv. Mater.* **1994**, *6*, 491.
- [14] K. Saxena, V. K. Jain, D. S. Mehta, *Opt. Mater.* **2009**, *32*, 221.
- [15] N. K. Patel, S. Cinà, J. H. Burroughes, *J. Sel. Top. Quantum Electron.* **2002**, *8*, 346.
- [16] Y. Kawamura, K. Goushi, J. Brooks, J. J. Brown, H. Sasabe, C. Adachi, *Appl. Phys. Lett.* **2005**, *86*, 071104.
- [17] A. P. Green, A. R. Buckley, *Phys. Chem. Chem. Phys.* **2015**, *17*, 1435.
- [18] J. C. De Mello, H. F. Wittman, R. H. Friend, *Adv. Mater.* **1997**, *9*, 230.
- [19] Y. Zhang, J. Lee, S. R. Forrest, *Nat. Commun.* **2014**, *5*, 1.